Acta Materialia 200 (2020) 328–337

Contents lists available at ScienceDirect

Acta Materialia

journal homepage: www.elsevier.com/locate/actamat

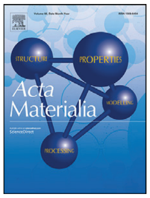

Full length article

Mapping the kinetic evolution of metastable grain boundaries under non-equilibrium processing

Zhitong Bai [a], Glenn H. Balbus [b], Daniel S. Gianola [b], Yue Fan [a,*]

[a] Department of Mechanical Engineering, University of Michigan, Ann Arbor, MI 48109, USA
[b] Materials Department, University of California, Santa Barbara, CA 93106, USA

ARTICLE INFO

Article history:
Received 9 May 2020
Revised 2 September 2020
Accepted 4 September 2020
Available online 10 September 2020

Keywords:
Metastable grain boundaries
Non-equilibrium kinetics
Ageing/rejuvenating crossover
Atomistic modeling
Potential energy landscape

ABSTRACT

The kinetic evolution of a multiplicity of metastable grain boundaries (GBs) under fast driving conditions are studied by atomistic modeling. Assisted with an enhanced statistical analysis, the energetic evolution of GBs over a broad metastability-temperature space is mapped out, wherein two distinct regimes—an ageing regime and a rejuvenating regime—are retrieved with high fidelity. By comparing the results under various conditions (*e.g.* random perturbations, isothermal annealing, and fast heating/cooling), it is shown that such ageing/rejuvenating mechanism map is universal, irrespective of the actual stimuli used to elicit the metastable GBs. The ageing/rejuvenating phenomena are demonstrated to stem from the energy imbalance of uphill climbing and downhill dropping during sequential transitions in the system's potential energy landscape. Without the necessity of introducing free parameters, such model can reconcile experimentally measured hardness variation of nanocrystalline metals subjected to femto-second laser irradiation, and it therefore provides a novel perspective on achieving a plurality of interfacial states and facilitating previously inaccessible property regimes.

1. Introduction

Polycrystalline solids are among the most pervasive engineering materials, and the interfaces between the grains, known as grain boundaries (GBs), play a decisive role in determining the system's physical properties [1,2]. In recent years, nanocrystalline (NC) alloys have received considerable attention, because the high concentration of GBs endows the systems with high strength [3–6], improved resistance to wear [7] and fatigue [8], and in some instances high ductility [9].

Traditionally, the structure and properties of a given GB are characterized by five angular degrees of freedom between the neighboring crystals. While this macroscopic description of GBs is powerful, it does not uniquely and completely describe the atomistic structure of the GB. To be more specific, GBs' microscopic configurations are typically isolated by identifying the structures with minimum energy at 0 K. These structures are usually associated with high coherency and distinguishing structural units, *e.g.* kites [10–12] or misfit dislocation arrays [13,14]. However, such "ideal" equilibrium GBs with "frozen" microstructures are too often oversimplified and do not capture the complex behavior of GBs under realistic environments [1].

Recent computational studies by Han and Srolovitz [15] have systematically demonstrated that GBs, even with a fixed misorientation, can exhibit an essentially infinite number of metastable states with a broad and continuous spectrum of energies. It has also been demonstrated that the NC alloys' enhanced fatigue toughness [8] and record-breaking combination of strength and ductility [9] may in fact originate from intentionally introducing disorder within the GB regions. Moreover, recent sub-ablation femtosecond (*fs*) laser experiments [16] show that NC samples could experience a significant hardness variation (up to 87%) following laser pulses with negligible grain sizes changes. These studies collectively underscore the pressing need for a fundamental knowledge on the evolution of non-equilibrium metastable GBs' under external stimuli.

In the present study, we introduce random perturbations to a group of ⟨100⟩ symmetric tilt grain boundaries (STGBs) in Cu to create a multiplicity of metastable states with broad energy distributions, mimicking the consequences of ultrafast external stimuli (*e.g.* *fs*-laser pulses). We then investigate those metastable GBs' energetic temporal evolution under the condition of isothermal annealing over a broad temperature range from 0 to 0.95 T_m. In conjunction with effective data mining a high-fidelity mechanism map is constructed, showing that the evolution of metastable GBs over

---

[*] Corresponding author.
E-mail address: fanyue@umich.edu (Y. Fan).

https://doi.org/10.1016/j.actamat.2020.09.013
1359-6454/

a broad energy-temperature space can be distinctly divided into an ageing regime, and a rejuvenating regime, respectively. It is further demonstrated that such ageing/rejuvenating stems from the energy imbalance during the elementary transitions between local minima in the system's underlying potential energy landscape (PEL), similar to that in metallic glasses. Such a physical picture enables an effective description of the energetic and mechanical responses of metastable GBs to external stimuli without the necessity of invoking free fitting parameters, and it successfully captures both the non-linear hardness variation of NC alloys under *fs*-laser pulses and its dependence on the samples' processing history [16].

2. Materials and methods

A realistic embedded atom method (EAM) inter-atomic potential [17] for Cu is employed in atomistic simulation for the construction and investigation of GBs in the present study. At first, the "ground-state" configurations for a group of $\langle 100 \rangle$ STGBs are created through a conventional bicrystal set-up: the symmetrically tilted upper and lower grains are joined together, followed by in-plane rigid body translations, atom deletions, and finally a conjugate gradient minimization [18]. The sizes of simulation boxes vary from 23,840 to 135,200, depending on the specific misorientation angles (more details in Appendix, Table B1).

Random perturbations are then introduced to the hereby constructed ideal GBs to mimic the consequences of fast external stimuli. Specifically, a thin plate section near the GBs (between −7 Å and 7 Å along the normal direction) is selected, and atoms therein are randomly chosen and displaced to a random position. By minimizing the system after each random perturbation, a multiplicity of metastable structures and their corresponding energies can thus be obtained. Note that the atom numbers are kept constant during the metastable GBs creation process, because in the scope of present study the system is driven out of equilibrium under ultrafast stimuli (*e.g.* sub-ablation *fs*-laser pulses) and thus should no longer be characterized by a grand canonical ensemble.

The energetic and structural evolutions of metastable GBs under both isothermal annealing and fast thermal-cycling conditions are investigated by molecular dynamics (MD) simulations using the LAMMPS software. For isothermal annealing studies, the system is annealed at a constant temperature with the NPT ($P = 0$) control for 500 *ps*. The time step is set to be 2 *fs*. The energy and structure of the system are calculated every 1 *ps*. For fast thermal-cycling studies, the metastable GBs' energy and configurations are tracked every 5 *K*. The energy of a metastable GB is calculated as the excess energy of the present configuration divided by the area of grain boundary plane, where the excess energy is defined as the energy difference between the GB system's potential energy and the potential energy of a single crystal system with the same number of atoms.

The activation relaxation technique (ART) [19] is also employed in sampling the PEL of metastable GBs and obtaining their activation energy spectra. Specifically, the ART simulation is initiated by choosing a random atom inside the GBs, which has been characterized as the particles with a centro-symmetry parameter (implemented in LAMMPS) larger than 2.0. Then small perturbations, *i.e.* random displacements, were applied to the central atom and its nearest neighbors with a total displacement of 0.5 Å. When the lowest eigenvalue (*i.e.* curvature) of the PEL calculated by Lanczos algorithm is found to be smaller than -0.01 eV $\AA^{-2}$, the system is then relaxed toward the saddle point with a force tolerance of 0.005 eV $\AA^{-1}$. For each central atom, 10 ART searches with different perturbation directions are applied. Finally, statistical histograms are obtained by removing the repeated and failed searches.

3. Results and discussion

3.1. GBs' metastability evolution in energy-temperature space

Infinite number of metastable GBs with various energy states can be created through the random perturbations described above in Section 2, and the left panel in Fig. 1 shows 4 representative structures after perturbing the ideal Σ5 (310) STGB. The hereby obtained metastable structures are then subjected to isothermal annealing at various temperatures below the system's melting point (T_m~1350 *K*), and the corresponding energetic temporal evolution curves are tracked, as seen in the right panel of Fig. 1. To

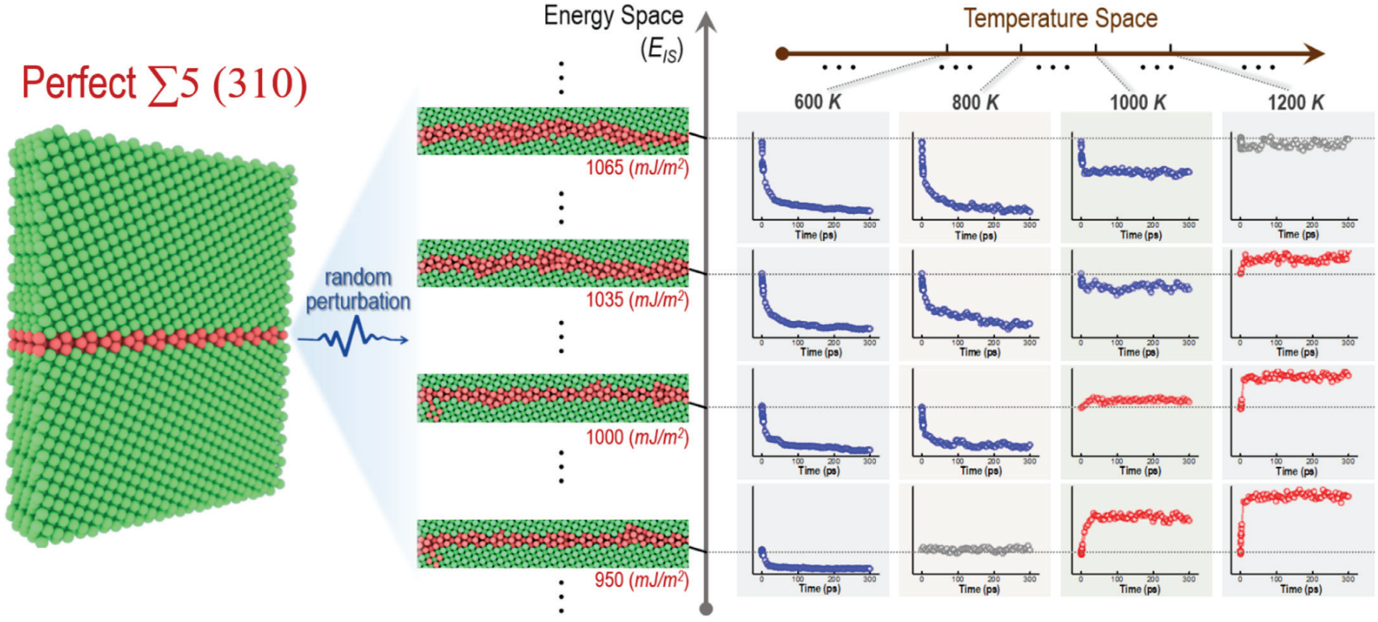

Fig. 1. (Left) A multiplicity of metastable Σ5 (310) GBs across a broad energy range are created by introducing random perturbations to the ideal ground-state GB. (Right) The produced metastable structures are then subjected to isothermal annealing at various temperatures from 0 *K* to 1300 *K* (below the system's melting point, T_m~1350 *K*), and the corresponding energetic temporal evolution curves are tracked.

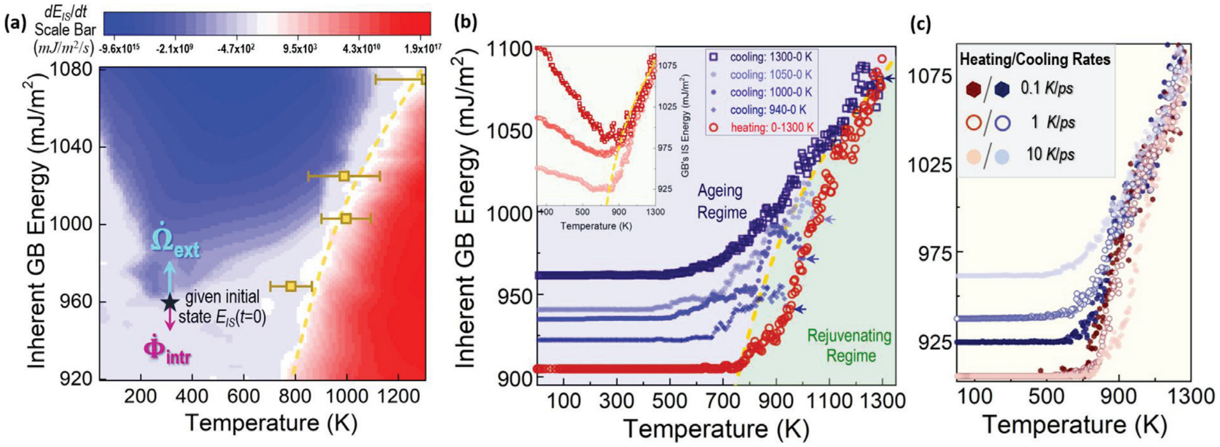

Fig. 2. (a) Resolved pixel map of GB's energetic variation rate in the broad energy-temperature space. In the red regime $(\partial E_{IS}/\partial t)|_T > 0$, and the system exhibits a rejuvenating behavior; while in the blue regime $(\partial E_{IS}/\partial t)|_T < 0$, and the system exhibits an ageing behavior. The ageing/rejuvenating crossover boundary is marked by the dashed yellow curve. The open yellow squares with error bars are the numerically calculated solutions to $\bar{E}_A(T) - \bar{E}_R = 0$, provided with the E_A and E_R spectra at different energy levels in the system's underlying PEL. (b) MD validations on GB's metastability evolution under fast heating-cooling cycles at the rate of 10 *K/ps*. The anomalous peaks in the truncated thermal cycles (*i.e.* heating/cooling switching at intermediate temperatures of 940 K, 1000 K, and 1050 K marked in the plot) overlap well with the dashed yellow curve extracted from (a), suggesting the validity of the obtained ageing/rejuvenating mechanism map. Inset plot shows the energetic evolution of a few metastable states with higher initial energy levels during heating at 10 *K/ps*. The system's IS energy keeps decreasing in the early stage until it hits the dashed yellow curve, and then the system's IS energy starts to increase afterwards. (c) The heating/cooling cycles at different rates in MD simulations. The hysteretic behavior remains, while its magnitude becomes smaller at lower rates. (For interpretation of the references to colour in this figure legend, the reader is referred to the web version of this article.)

better analyze the GBs' evolution, we herein adopt the quenching protocol used by Zhang and Srolovitz [20] and focus on the variation of the GBs' inherent structures (ISs) energy. Note that the ISs are obtained by minimizing the dumped configurations to 0 *K* with a steepest descent algorithm, and the real dynamics at finite temperatures are not interrupted.

It is evident in Fig. 1 that the evolution of a metastable GB is sensitively dependent on both its IS energy (denoted as E_{IS}) and surrounding temperature. In some parameter space (blue curves), E_{IS} decreases to a lower level during annealing, which essentially represents an ageing phenomenon; while in some other parameter space (red curves), E_{IS} increases as a function of time, which corresponds to a rejuvenating behavior. Under some specific cases (grey curves), GBs reach a steady state condition with the E_{IS} being invariant with annealing time. To avoid the plot being too crowded in Fig. 1 we only display the evolution of 4 representative metastable GBs at 4 different temperatures. Many more metastable states have actually been considered in the present study over many more assigned temperature conditions, and we note that they all share the qualitatively similar complexity.

3.2. Mapping of ageing and rejuvenating

Fig. 1 suggests that metastable GBs' energetic evolution is intrinsically non-linear and non-monotonic. To better understand such behavior subjected to complex conditions, it is critical to quantify their intrinsic ageing/rejuvenating rate. The energy variation rate can be calculated by analyzing the time derivative of the isothermal annealing curves $(\partial E_{IS}/\partial t)|_T$, at various prescribed (E_{IS}, T) conditions. Using an enhanced statistical analysis to examine the evolution of all the generated metastable GBs (see Supplementary Materials Fig. S1 for details), a high-fidelity pixel-wise map on the energy variation rate is constructed in Fig. 2a across a broad parameter space.

For the convenience of visualization, each pixel comprising the map is colored on a log scale according to its energy variation rate. At first, it is immediately apparent from Fig. 2a that the evolution of metastable GBs can be divided into two distinct regimes, namely an ageing regime (blue) where$(\partial E_{IS}/\partial t)|_T$is negative and a red regime where $(\partial E_{IS}/\partial t)|_T$becomes positive. The crossover boundary is marked by the dashed yellow curve, indicating the steady state condition. Another intriguing observation is that, the contour lines in the blue regime exhibit a non-monotonic dependence on temperature, indicating an optimized condition for the ageing of metastable GBs to take place.

It is worth noting that, Fig. 2a is constructed upon the isothermal annealing analyses independently from any special/extreme driving forces. In other words, such a map reflects generally the metastable GBs' energetic evolution at various prescribed (E_{IS}, T) conditions. Therefore, to validate the demarcation of ageing and rejuvenating regimes given by Fig. 2a, the two most straightforward approaches one can consider is to introduce external stimuli either along the E_{IS}-axis or along the T-axis. The E_{IS}-axis examination will be discussed later in Section 3.4, and here in this section we introduce the T-axis stimuli to verify Fig. 2a through a series of heating/cooling MD simulations.

Specifically, in Fig. 2b the initial ground-state $\Sigma 5$ (310) GB is heated to 1300 *K* (red open circles) at a rate of 10 *K/ps*, which is then immediately followed by a cooling treatment to 0 *K* (dark blue open squares) at the same rate. Overall, there exhibits a clear hysteretic behavior, which is not surprising because the GB is driven away from equilibrium by the ultrafast processing and eventually trapped at a metastable state. More specifically, in the heating stage the system's IS energy does not substantially increase until it goes beyond the crossover boundary (dashed yellow curve) and enters the rejuvenating regime previously identified in Fig. 2a. Between 1100 *K* and 1300 *K* the data points overlap with the dashed yellow curve, because at high temperatures the intrinsic relaxation dynamics becomes fast enough and the system is able to remain at steady state. Upon cooling from high temperatures, the dark blue squares are located consistently on the left side of the crossover boundary and exhibit a monotonic decreasing (*i.e.* ageing) behavior, corroborating the mechanism map in Fig. 2a. The heating/cooling rate effects are examined in Fig. 2c at lower rates of 1 *K/ps*, and 0.1 *K/ps*, respectively. The hysteretic behavior clearly remains, although the apparent magnitude of hysteresis becomes smaller at a lower heating/cooling rate because it would provide more time for the system to relax towards the equilibrium. Admittedly, the heating/cooling rates in MD simulations are extremely fast. But it is not impossible to benchmark the MD results by realistic experiments. For example, electrical pulse technique can reach an effective cooling rate of 10^{14} K/s [21] that is even shorter than typical MD timescales, although such a comparison is beyond the scope of the present study. We also note that, while the magnitude varies, such hysteresis is universal in a diversity of other $\langle 100 \rangle$ STGBs (see Appendix, Fig. B1).

To further verify the ageing/rejuvenating mechanism map, we truncate the full thermal cycle and instead begin the cooling treatment at intermediate temperature, *e.g.* 940 *K*, 1000 *K*, and 1050 *K* marked in Fig. 2b. An anomalous behavior occurs under such scenarios. Specifically, the energy first increases despite the decreasing temperature, reaching a peak value below the temperature where the simulation is truncated. It therefore suggests that, on the right side of those anomalous peaks there is $(\partial E_{IS}/\partial t)|_T > 0$, while on the left side there is $(\partial E_{IS}/\partial t)|_T < 0$. It is evident that those peak positions are well located on the crossover boundary extracted from Fig. 2a. The inset plot in Fig. 2b presents another set of MD validation by heating (at 10 *K/ps*) a few selected metastable GBs with higher initial energy states. It is clear that the energy decreases first and then increases, and transitioning points of such non-monotonic variations align well again with the extracted yellow curve from Fig. 2a. The extent of such agreement suggests that the hereby discovered ageing/rejuvenating mechanism map is rather universal, irrespective of the actual stimuli used to elicit those non-equilibrium GB structures. As discussed below, this would also lay the foundation to describe and explain the mechanical behavior of NC alloys under *fs*-laser irradiation.

3.3. PEL origin of the non-equilibrium evolution

In pursuit of explaining the underlying physics of the obtained mechanism map, here we adopt a PEL perspective because the time evolution of a condensed matter system and any concomitant property changes are known to correspond to the transitions between local minima and progressive exploration of different ISs in the system's underlying PEL [22–29]. Note that a similar ageing/rejuvenating behavior has been recently reported in metallic glasses [30], and it is demonstrated there that the crossover boundary can be well characterized by the competitions between an effective uphill climbing energy ($\bar{E}_A$) and a downhill dropping energy ($\bar{E}_R$) during sequential transitions in the system's potential energy landscape. In particular, when $\bar{E}_A < \bar{E}_R$ the system would evolve towards a lower energy state and thus undergo an ageing process; otherwise, an opposite rejuvenating effect would occur. Given the many reported similarities between glasses and GBs [31–35], here we seek to employ such an energy imbalance criterion to interpret the resolved map in Fig. 2a. Specifically, the effective $\bar{E}_A$ and $\bar{E}_R$ are calculated as [30]:

$$\bar{E}_A(T)|_{IS} = -k_B T \cdot \ln\left[\int P(E_A)|_{IS} \cdot e^{-\frac{E_A}{k_B T}} dE_A\right] \tag{1}$$

$$\bar{E}_R|_{IS} = \int E_R \cdot P(E_R)|_{IS} dE_R \tag{2}$$

Note that because in GB systems each IS can be connected with many different saddle states, all those potential pathways in the PEL [36] need to be taken into consideration. Therefore, instead of being explicit numbers, the effective $\bar{E}_A$ and $\bar{E}_R$ have to be estimated over the broad distributions, $P(E_A)|_{IS}$, and $P(E_R)|_{IS}$, respectively, which are dependent on the system's present IS. The key difference above is that $\bar{E}_A$ is *T*-dependent, while $\bar{E}_R$ is *T*-insensitive. This is because the up-hill climbing is a thermally activated process, while the down-hill dropping can spontaneously happen and does not need thermal assistance [30].

One can analytically prove that $\bar{E}_A(T)|_{IS}$ in Eq. (1) is monotonically increasing as a function of *T*. Therefore, it is expected that the term $(\bar{E}_A - \bar{E}_R)$ would flip from negative to positive as *T* increases, naturally explaining the transition from ageing to rejuvenation in Fig. 2a. More quantitatively, the ageing/rejuvenating crossover should occur when $\bar{E}_A(T) - \bar{E}_R = 0$. Therefore, according to Eqs. (1-2), a precise quantification of the crossover point relies on the determination of accurate spectra of $P(E_A)|_{IS}$ and $P(E_R)|_{IS}$. Here we employ the ART method mentioned in Section 2 to obtain such spectra, which is known as an effective atomistic sampling algorithm capable of probing the PEL structures with high fidelity [19,37–39].

Fig. 3.a shows the obtained spectra of E_A and E_R at 4 different IS energy levels: 1075 mJ/m^2, 1025 mJ/m^2, 1003 mJ/m^2, and 968 mJ/m^2. The distribution $P(E_A)|_{IS}$ shows an apparent dependence on the GBs' IS energy level: as E_{IS} decreases, the fractional distribution of low energy activation values becomes smaller, resulting in a larger average E_A. On the other hand, $P(E_R)|_{IS}$ is evidently IS-independent and follows a universal exponential decaying distribution, reminiscent of similar features in glassy materials [30,38]. The computed spectra of $P(E_A)|_{IS}$ and $P(E_R)|_{IS}$ are then fed into Eqs. (1-2) for numerical calculations, and by varying the temperature one can thus identify when the crossover condition (*i.e.* $\bar{E}_A(T) - \bar{E}_R = 0$) is satisfied. The open yellow squares in Fig. 2a represent such PEL-enabled calculations, which are consistent with the independent annealing studies within numerical error. Such agreement is encouraging, as it lends credence to the notion that the nature of the GBs' ageing/rejuvenation originates from the kinetic processes in the underlying PEL.

It is also worth noting that the broad E_A spectra approximately consist of two modes: a distribution centered around 0.6 *eV*, and another complementary mode distributed within the lower energy tail. These seem to correspond to the reported activation barriers for GBs' self-diffusion [40,41], and the collective reshuffling processes [40], respectively. In other words, the entire spectrum of the GBs' migration/diffusion mechanisms are implicitly encoded in the PEL. Another noteworthy feature is that the activation energy spectra seem to be sensitive only to the energetics of GBs' IS rather than its detailed atomic configuration. To be more specific, in each panel of Fig. 3.a we show the spectra of two metastable GBs at the same energy level but with different atomic structures (Fig. 3.b), and the spectra are evidently similar to each other. As discussed later, this might lead to a vast simplification in building an explicit expression of $P(E_A)$ for metastable GBs.

The non-monotonic ageing phenomenon discussed above in Fig. 2a can also be readily explained by such a PEL picture. Specifically, the system's overall metastability evolution should be mutually determined by a driving factor, and a kinetic factor, respectively. The driving force factor, namely $(\bar{E}_A - \bar{E}_R)$, determines the direction/sign of the evolution. As discussed above, in the blue regime the sign of $(\bar{E}_A - \bar{E}_R)$ is negative while its absolute value keeps decreasing as *T* increases. On the other hand, the kinetic factor in general exhibits a monotonic increasing dependence on *T*. Such opposite sensitivities to temperature yield the observed non-monotonic contour lines in ageing regime. These collective results point to a wholly consistent viewpoint of metastable GBs' energetics and their evolutions.

3.4. Implication on the mechanical behavior of GBs

The mechanical behavior of nanocrystalline materials is inherently linked to the energetic state of GBs in the limit where deformation mechanisms become increasingly GB-mediated. Work from Vo [42] et al. demonstrated that, for a fixed grain size, the

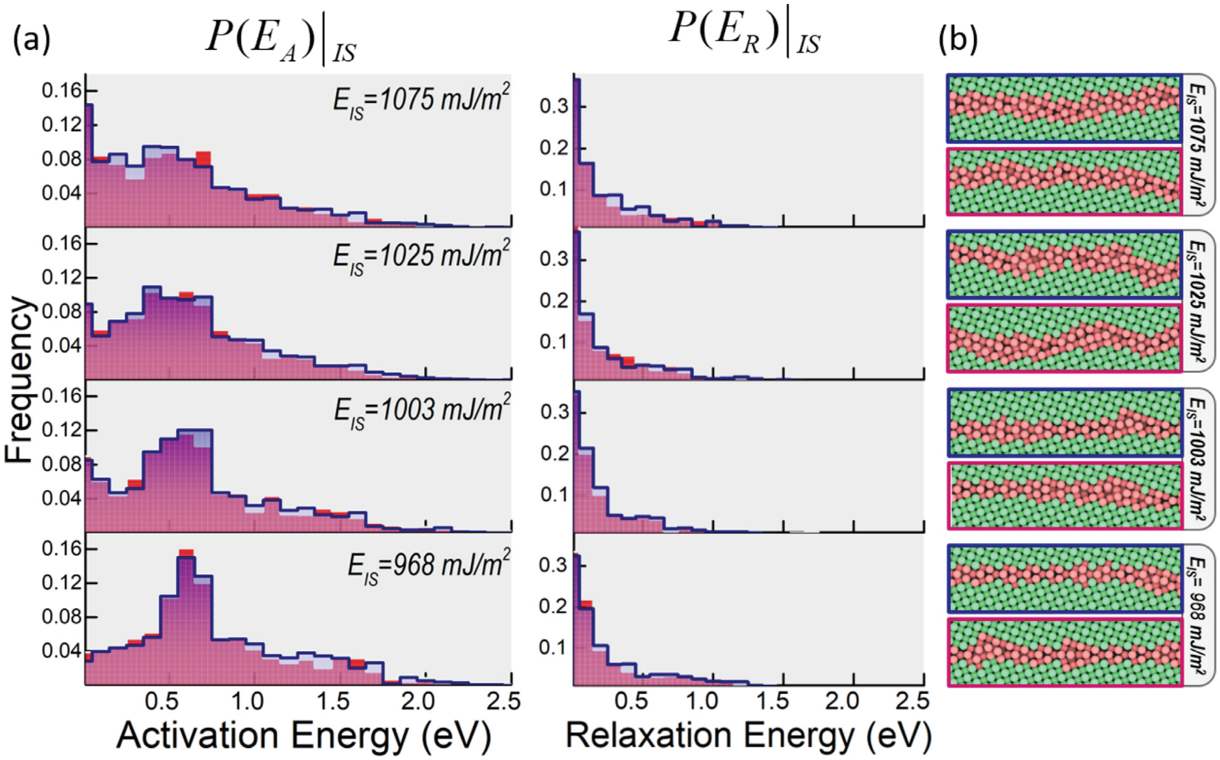

Fig. 3. (a) The ART-probed E_A and E_R spectra of metastable GBs at different energy levels by sampling the system's underlying PEL. In each panel it displays the spectra of two metastable GBs at the same energy level but with different atomic configurations shown in (b).

yield strength of nanocrystalline Cu is inversely proportional to the GB energy. Other simulations have demonstrated that during the deformation of metastable GBs, mechanisms such as GBs sliding are preferred over traditional dislocation plasticity, which in turn dramatically affects the mechanical properties [43]. Even in cases where dislocations participate in plastic deformation via GB emission and absorption mechanisms, their nucleation and propagation barriers as well as their ability to annihilate at GBs are influenced by the interface energies. Indeed, experimental evidence supports the observation that the hardness of a GB-concentrated system varies inversely as a function of its energy level [16]. Therefore, the PEL framework discussed above allows for a prediction of the GBs' mechanical performance at different conditions. We focus on recent experiments showing GB rejuvenation using ultrafast (*fs*) laser pulses, which result in dramatic changes in the material hardness [16].

The interactions between *fs*-lasers and materials are rather complex, but several insights relevant to the present work can be gleaned. On the one hand, extremely fast temperature variations can be involved. Although the heating and cooling rates during sub-ablation threshold *fs*-laser experiments (focused in the present study) have not been investigated, simulations of high-energy *fs*-laser irradiation that induce material ablation demonstrate heating and cooling rates upwards of 10^{11} K/s during the ablation process [44,45]. While the relaxation phenomena present in sub-ablation *fs*-laser irradiation is similar to that during ablation, as no material is removed during experiments we do not anticipate such high temperatures or heating rates, although modeling efforts to investigate such phenomena would make for intriguing future work. Despite limited understanding of the temperature effects in this regime, sub-ablation *fs*-laser irradiation results in *GPa*-level tensile and compressive stress waves localized to GBs that may induce localized atomic rearrangements [16,46], effectively increasing the energy of GBs regardless of the thermal profile. Thus, while it is intractable to experimentally measure the effective heating/cooling rates during sub-ablation *fs*-laser irradiation, the net result of such irradiation should be an overall increase in the energetic state of the GBs at a fixed temperature, as evidenced by the dramatic decrease in hardness. Considering these points, the system's energetic evolution in the presence of external stimuli, as illustrated in Fig. 2a, should then be determined by the interplay between two factors, namely the intrinsic energy variation $\dot{\Phi}_{\text{intr}}(E_{IS}, T) \propto (\bar{E}_A - \bar{E}_R)$, and the external energy input rate $\dot{\Omega}_{ext}$ (*i.e.* net results of sub-ablation *fs*-laser irradiation discussed above), respectively.

While an analytical expression of $\dot{\Phi}_{\text{intr}}(E_{IS}, T)$ is not yet available, its numerical value over broad E_{IS}—T space can be obtained by interpolating the high-resolution pixel map in Fig. 2a. Therefore, using experimentally-relevant values of $\dot{\Omega}_{ext}$(*e.g.* the power of the *fs*-laser pulse) and the GB's initial energy state $E_{IS}(t = 0)$, one can then numerically resolve the GBs' metastability evolution. The qualitative picture is clearly captured in Fig. 2a: if the external stimuli $\dot{\Omega}_{ext}$is larger than the intrinsic ageing (*i.e.* energy dissipation) $\dot{\Phi}_{\text{intr}}$, then the system will move upwards on the map. However, such an energy increase will not be maintained at a constant rate because, as E_{IS} increases, the intrinsic term $\dot{\Phi}_{\text{intr}}$ becomes larger, resulting in a slower net gain rate of E_{IS}. When absolute values of the intrinsic and external terms become equal, the system reaches a steady state and the energy is stabilized at a saturated level. From a more quantitative perspective, the system's metastability evolution and the resultant mechanical behavior would be determined by the initial energy state, the stimuli strength, and temperature.

Fig. 4 shows the GB's energetic evolution at room temperature and under an external stimulus of 1.0×10^{14} $mJ/m^2/s$. The choice of $\dot{\Omega}_{ext}$is rationalized after considering the *fs*-laser's pulse energy, pulse width, and volume fraction of affected GBs in real experi-

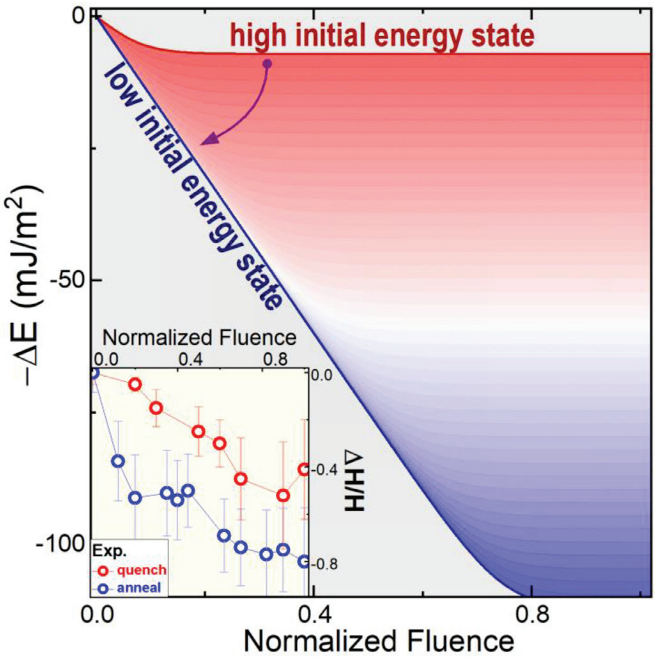

Fig. 4. Numerically calculated GBs' energetic evolution under the external stimuli of 1.0×10^{14} $mJ/m^2/s$. Here we plot the inverse variation of energy (-ΔE) for the convenience of comparison with the sample's hardness, which is known inversely proportional to GBs' energy. In general, the curves show a non-linear stiff-to-flat variation pattern. In addition, a sample with lower initial energy state can accommodate more variation as opposed to a sample with higher initial energy state. Such predicted features are in good agreement with recent measurements on the hardness variation of the Cu-rich NC alloys under fs laser processing (details in Appendix A). (For interpretation of the references to colour in this figure legend, the reader is referred to the web version of this article.)

ments [16]. To facilitate the comparison with the hardness measurement here we plot the inverse variation of the system's energy (-ΔE) with respect to its initial state, because as discussed above, the hardness of a NC system is inversely proportional to the GBs' energy. In particular, we examined a series of cases with various initial energy states ranging from 960 mJ/m^2 and 1065 mJ/m^2. Two notable features emerge: (i) all curves show non-linear behavior with a gradually vanishing slope prior to saturation. This behavior has been discussed above – the net variation rate of E_{IS} becomes slower and slower under the driving of external stimuli. (ii) A sample with lower initial energy state can accommodate more uphill energy variation as opposed to a sample with a high initial energy state. If we convert these to hardness values, then one should expect that: (i) the sample's hardness should gradually reduce and eventually saturate with increasing laser fluence; and, (ii) the hardness drop in a sample with lower initial energy state is larger than that in a higher initial energy state sample. Note that while saturation is not always observed experimentally, as it sometimes is precluded by material removal (ablation) at higher laser energies, the predicted trends in Fig. 4 are consistent with the reported experimental measurements [16] on Cu-rich NC alloys (seen in the inset plot) and many other alloys reflecting a diverse range of GB chemistries and synthesis routes (see Supplementary Materials Fig. S2.)

It is also worth remarking that conventional wisdom states that NC materials soften after annealing owing to grain growth. However, an emerging body of experimental evidence highlights an initial regime of hardening with increasing annealing temperature, prior to softening at the onset of microstructural evolution [5,47–50]. While different origins (*e.g.* solute segregation and dislocation annihilation at GBs) have been proposed to explain such non-monotonic behavior, some studies [5,48] demonstrate that the anomalous hardening phenomenon still exists even in pure NCs and with a reduced dislocation density, suggesting that alternative mechanisms mediate this phenomenon. Fig. 2a in the present study places such an alternative perspective on a quantitative foundation. Specifically, the contour lines in the ageing regime present a clear non-monotonic feature as a function of temperature, meaning that at various annealing temperatures the system would be driven to different energy levels in a concave up shape. Consequently, the hardness should vary non-monotonically in a concave down manner, which is qualitatively consistent with the reported experiments.

We would like to clarify that here we do not directly focus on the specific strengthening and deformation mechanisms of NCs, such as nucleation of dislocations or disconnections [51–55]. Instead, we propose an energy-centric and statistical perspective to acquire a predictive implication on the metastable GBs' mechanical behaviors under various environments. The rationale behind such a perspective comes from the established fact [42,56,57] that the yield strengthen of NC alloys are strongly and inversely correlated with the GBs' energy. Interestingly, very recent studies [58] on the GBs containing both structural and chemical complexities also demonstrate that, from a statistical point of view it is the energetics, rather than detailed structural/chemical features, that governs the GBs' behaviors under driving conditions. Therefore, there is reason to believe the hereby developed energetic evolution model may be broadly applicable to the understanding of metastable GBs under non-equilibrium processing.

3.5. E_A spectra correlations between various metastable GBs

As discussed above, the energetic evolution and mechanical behavior of metastable GBs are dependent on the system's surrounding E_A spectrum in the PEL. A central question that follows is: are there unique structural signatures associated with the various GB states responsible for the spectrum of accessible behavior? The features of the activation energy spectra$P(E_A)|_{IS}$ provide an important clue. It is not difficult to imagine that, for a given GB's IS, there should be a corresponding$P(E_A)|_{IS}$. However, given the complex metastability of GBs [15], there are essentially infinite numbers of ISs and it would be impractical to sample all those spectra. Fig. 3 in the present study suggests a vast simplification of this problem. Specifically, in each panel of Fig. 3.a we show the spectra of two metastable GBs at the same energy level but with different atomic structures, and the spectra are very similar to each other. This implies that the E_A spectrum is only sensitive to the energetics of GBs' IS rather than its detailed atomic configuration. To further verify such hypothesis, we select multiple different metastable GBs over a broad range of energy scales and probe each of their E_A spectra using the ART method mentioned above in Section 2. Fig. 5 examines the contrasts between those spectra defined as $\Delta_{ij} \equiv (\int [P_i(E_A) - P_j(E_A)]^2 dE_A)^{1/2}$, where $P_i(E_A)$and $P_j(E_A)$correspond to samples #*i's* and #*j's* spectra, respectively. It is clear that, when two samples' E_{IS} are close to each other their activation energy spectra differences are relatively small; on the contrary, if the E_{IS} of two samples are far from each other, the spectra differences are relatively large. Such nice correlation indicates that it might be possible to express the E_A spectrum as an explicit function of E_{IS}, $P(E_A|E_{IS})$. Although obtaining a reliable formalism for $P(E_A|E_{IS})$ is beyond the present work's scope, it represents a rich avenue for future inquiry because of its potential in leading to a reduced-order modeling approach for disordered material systems.

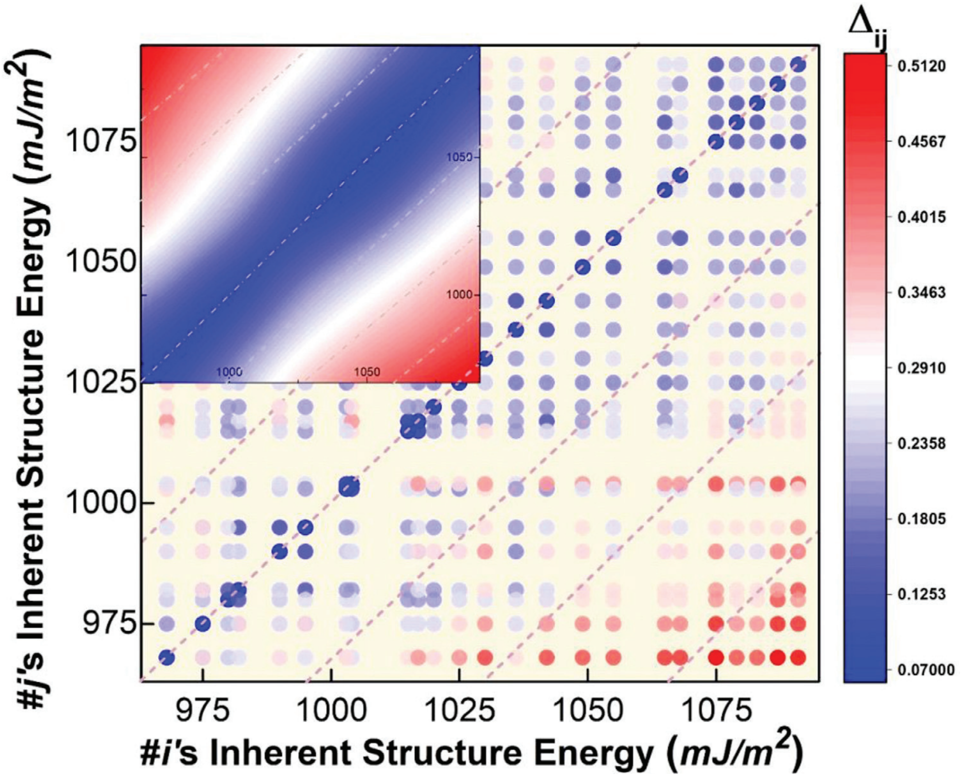

Fig. 5. The differences between the E_A spectra among a number of metastable GBs. It is found that if two GBs' IS energies are close to each other, their E_A spectra differences are also smaller (diagonal blue data), while the opposite is true if two GBs' IS energies are far from each other (off-diagonal red data). The discrete data points are converted into the inset contour map using the thin-plate spline interpolation algorithm. (For interpretation of the references to colour in this figure legend, the reader is referred to the web version of this article.)

3.6. Further discussion

It would be of interest to ask whether the effective model developed above for metastable GBs can be applicable to those ground state GBs (*e.g.* perfect straight interfaces with repeating kites), and we believe the nature of E_A distribution plays an important role. More specifically, general metastable GBs contain significant disorder and their E_A spectra are usually wide, continuous, and stretch to very low barrier (almost zero), as seen in Fig. 3a. By contrast, for ground state GBs their E_A distributions should present in a much more discrete pattern with a well-defined lower bound. For example, it has been reported [36] that the E_A distribution in a perfect $\Sigma 5$ GB in Cu displays a clear onset threshold barrier around 0.6 *eV*. This is not so surprising because the apparent order in perfect GBs (*e.g.* repeating kites) would impose strong restrictions and thus considerably reduce the number of available transition pathways in the PEL. According to Eq. (1), a threshold of 0.6 *eV* for $P(E_A)$ distribution means the effective activation barrier $\bar{E}_A$ can only be even higher, which is significantly larger than the effective $\bar{E}_R$ in Fig. 3b. In other words, from a statistical point of view $(\bar{E}_A - \bar{E}_R)$ should always be greater than 0 in this case, suggesting the system can only move up (rejuvenation) while moving down (ageing) is practically prohibited. This actually complies with the definition of the "ground" state.

In spite of its qualitative compliance, one should not overstate the applicability of the present study onto ground state GBs. This is because Eq. (1) is actually derived after statistical average and thus holds a mean-field spirit. In other words, its robustness might be compromised in the absence of a wide and continuous E_A spectrum. Therefore, we believe the framework developed in the present study is more suitable to investigate general metastable GBs rather than perfect ground-state GBs.

As a final note, the hereby discovered ageing/rejuvenating evolution map for metastable GBs, and the dependence of their activation barrier spectra on E_{IS}, are strongly reminiscent of the recently observed non-equilibrium evolution in metallic glasses [30]. This is not surprising, as many previous studies have also reported the qualitative similarities between GBs and fully amorphous glassy materials [31–34,59]. However, we would like to remark that, the robustness of Eqs. (1-2) demonstrated in the present study lends quantitative credence to these similarities, which have not been fully characterized before. Even though the herein employed EAM potential is, in principle, empirical, the spectra of $P(E_A)|_{IS}$ and$P(E_R)|_{IS}$presented in Fig. 3.a are directly obtained using an atomistic algorithm rather than through a numerical fitting with free parameters. Given this, we see considerable promise in such a "bottom-up" PEL-oriented model for establishing quantitative structure-property relationships in metastable GBs and other disordered non-equilibrium materials.

4. Conclusions

Our present studies on the metastability evolution of bicrystal-GBs subjected to non-equilibrium conditions allow us to draw the following conclusions:

1. The energetic evolution of metastable GBs over the broad E_{IS}—T parameter space can be distinctly divided into an ageing regime $(\partial E_{IS}/\partial t)|_T < 0$, and a rejuvenating regime $(\partial E_{IS}/\partial t)|_T > 0$, respectively.
2. Such ageing/rejuvenating mechanism map is universal, irrespective of the actual stimuli used to elicit the metastable GBs.
3. The ageing/rejuvenating crossover stems from the energy imbalance during the elementary transitions in the PEL, which can be characterized by an effective kinetic model.

4. Without invoking free fitting parameters, such kinetic model is able to capture the energetic and mechanical responses of metastable GBs to external stimuli. It can naturally explain the intriguing phenomena observed in recent *fs*-laser experiments, namely the non-linear dependence of hardness variation on the laser fluence and the processing history effect.

We would like to note that many studies have demonstrated the strong correlations between GB relaxation and the mechanical performance of NC alloys [42,56,57]. Therefore, the capabilities established in the present study might provide a new perspective on controlling kinetic pathways for achieving a plurality of interfacial states with desired mechanical performance.

Declaration of Competing Interest

The authors declare that they have no known competing financial interests or personal relationships that could have appeared to influence the work reported in this paper.

Acknowledgment

The authors thank D. Rodney for insightful comments and discussions. This work was funded by NSF DMR-1944879. GHB was supported by a NSF GRFP Award No. 1650114. DSG's contribution is based upon work supported by the U.S. Department of Energy's Office of Energy Efficiency and Renewable Energy (EERE) under the Advanced Manufacturing Office Award Number DE-EE0009114.

Appendix A. Experimental

A.1. Sample fabrication

NC Cu-Zr samples were prepared from 99.99% pure Cu and 99.5% pure Zr powders in a SPEX 8000 M high-energy ball mill under Ar atmosphere. Samples were then annealed for 1*hr* at 950 °C, and then either quenched (Q) or slowly cooled (SC) to room temperature. Additional details of sample preparation for these materials can be found elsewhere [9,16].

A.2. Femtosecond Laser Irradiation

Femtosecond laser irradiation experiments were performed with a Clark MXR CPA-2110 Series Ti:Sapphire Ultrashort Pulse Laser with 1 kHz repetition rate, 780 nm wavelength, and 150 fs pulse width. All experiments were performed in air at room temperature. Regions of 0.1–0.5 mm^2 were exposed to single pulse fs-laser irradiation with ~30% overlap between subsequent pulses.

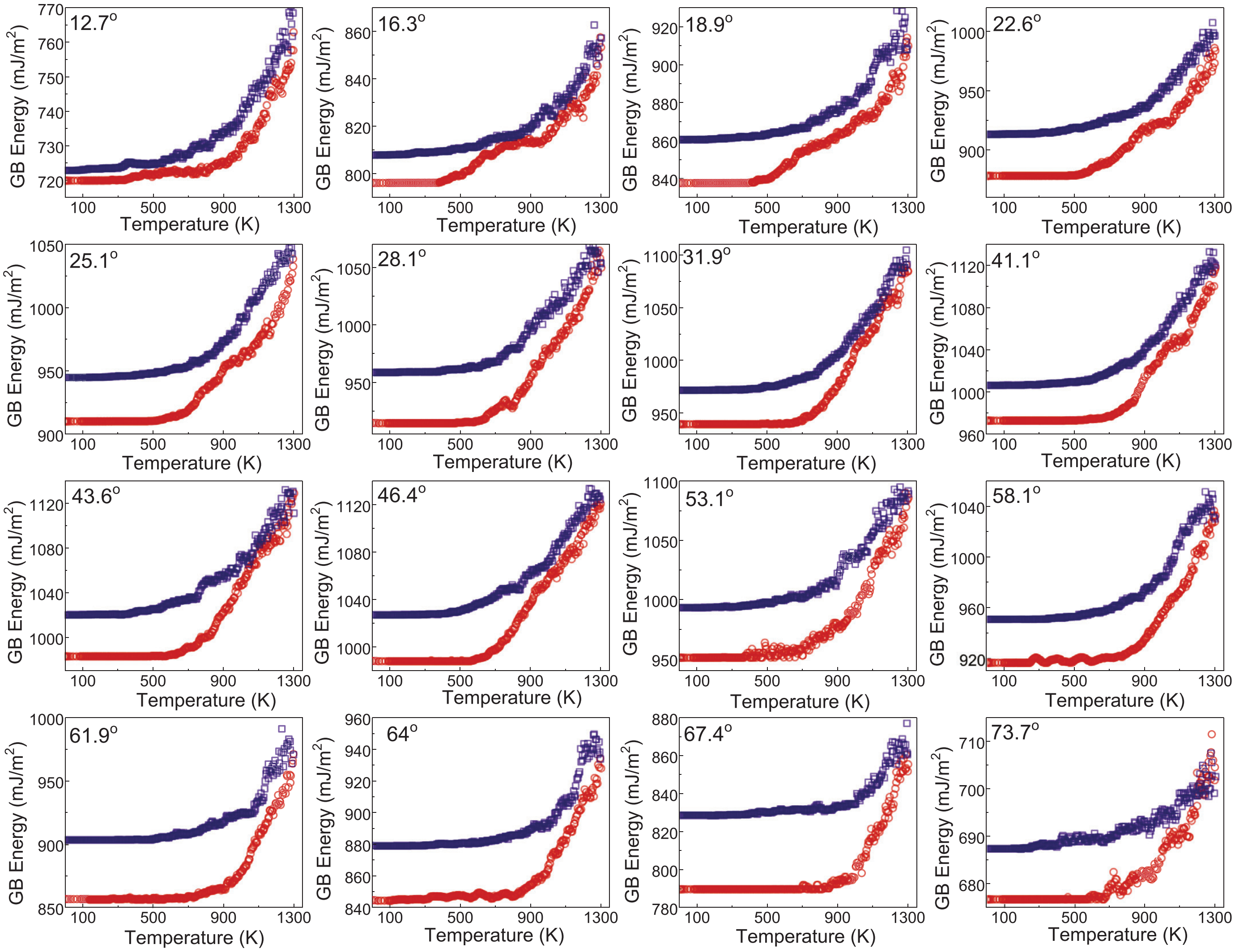

Fig. B1. Inherent energy evolution during the fast heating-cooling cycle for different STGBs with the misorientation angle ranges from 12.7° to 73.7° (the Σ5 (310) was shown in the main text and not displayed here.) The red open circles represent the heating stage and the blue open squares represent the cooling stage.

Table B1
The specifics on the dimension, atom number, and the IS energy before and after the fast thermal cycling for various ⟨100⟩ STGBs.

θ (°)	CSL	*x* (Å)	*y* (Å)	*z* (Å)	*# of Atom*	*E(H-0 K)* [mJ/m²]	*E(C-0 K)* [mJ/m²]
12.7	Σ41(019)	327.35	262.14	14.46	104,960	719.88	722.84
16.3	Σ25(017)	255.61	256.46	14.46	80,160	796.12	807.83
18.9	Σ37(016)	219.89	264.25	14.46	71,040	837.58	860.52
22.6	Σ13(015)	184.33	259.21	14.46	58,400	878.27	913.20
25.1	Σ85(029)	333.28	267.50	14.46	108,960	910.25	944.75
28.1	Σ17(014)	149.05	269.70	14.46	49,120	914.63	958.66
31.9	Σ53(027)	263.17	262.75	14.46	84,480	939.56	971.56
36.9	Σ5(013)	114.31	249.84	14.46	34,880	904.83	961.36
41.1	Σ73(038)	308.86	246.42	14.46	92,960	972.89	1006.39
43.6	Σ29(025)	194.67	273.12	14.46	64,960	983.11	1020.3
46.4	Σ29(037)	275.30	275.47	14.46	92,640	988.22	1027.27
53.1	Σ5(012)	80.83	241.52	14.46	23,840	951.2	993.46
58.1	Σ53(059)	372.18	297.26	14.46	135,200	916.59	950.88
61.9	Σ17(035)	210.78	251.60	14.46	64,800	856.53	903.65
64.0	Σ89(058)	341.03	272.17	14.46	113,440	844.56	879.24
67.4	Σ13(023)	130.34	262.14	14.46	41,760	789.78	828.75
73.7	Σ25(034)	180.75	254.14	14.46	56,160	676.79	687.46

Ablation thresholds were characterized on non-overlapping single pulse exposures via optical profilometry.

A.3. Indentation measurements

Indentation experiments were performed using a Nanomechanics iNano nanoindenter equipped with a 50 mN load cell and Berkovich tip. Prior to all indentation experiments, the tip area function was calibrated on a fused silica standard. Measurements were performed using a CSM indentation protocol, where a dynamic oscillation is imposed atop the loading curve, allowing depth-resolved hardness measurements [60]. All hardness measurements reported are extracted from ~ 30 nm penetration depths. Hardness values and errors reported are the mean and standard deviation, respectively, of at least 20 indentations.

Appendix B. Universal hysteresis of GBs with different misorientation angles

Fig. B1 below displays the IS energy responses of 16 additional ⟨100⟩ STGBs during fast thermal cycling from $0K \rightarrow 1300K \rightarrow 0\ K$ at a rate of $10\ K/ps$. The heating stage is shown by red open circles and the cooling stage is shown by blue open squares. Each data point in the plot is an average of three runs with the same condition. It can be seen that, while the rejuvenated IS energy might vary quantitatively, all the GBs considered here show a clear irreversible behavior, suggesting that the hysteresis during heating/cooling is a universal behavior of metastable GBs. Details of the specific dimensions, as well as the number of atoms and the GBs' IS energy before (H-0 K) and after (C-0 K) the fast thermal cycling with different misorientation angles are shown below in Table B1.

Supplementary materials

Supplementary material associated with this article can be found, in the online version, at doi:10.1016/j.actamat.2020.09.013.

References

[1] Y. Mishin, M. Asta, J. Li, Atomistic modeling of interfaces and their impact on microstructure and properties, Acta Mater 58 (null) (2010) 1117.
[2] A.P. Sutton, R.W. Balluffi, Interfaces in crystalline materials, Clarendon Press; Oxford University Press, Oxford, New York, 1995.
[3] M.A. Meyers, A. Mishra, D.J. Benson, Mechanical properties of nanocrystalline materials, Prog Mater Sci 51 (4) (2006) 427–556.
[4] L. Lu, X. Chen, X. Huang, K. Lu, Revealing the Maximum Strength in Nanotwinned Copper, Science 323 (5914) (2009) 607.
[5] J. Hu, Y.N. Shi, X. Sauvage, G. Sha, K. Lu, Grain boundary stability governs hardening and softening in extremely fine nanograined metals, Science 355 (6331) (2017) 1292.
[6] H. Van Swygenhoven, J.R. Weertman, Deformation in nanocrystalline metals, Materials Today 9 (5) (2006) 24–31.
[7] T.J. Rupert, C.A. Schuh, Sliding wear of nanocrystalline Ni–W: structural evolution and the apparent breakdown of Archard scaling, Acta Mater 58 (12) (2010) 4137–4148.
[8] J.D. Schuler, C.M. Barr, N.M. Heckman, G. Copeland, B.L. Boyce, K. Hattar, T.J. Rupert, In Situ High-Cycle Fatigue Reveals Importance of Grain Boundary Structure in Nanocrystalline Cu-Zr, JOM 71 (4) (2019) 1221–1232.
[9] A. Khalajhedayati, Z. Pan, T.J. Rupert, Manipulating the interfacial structure of nanomaterials to achieve a unique combination of strength and ductility, Nat Commun 7 (2016) 10802.
[10] A.P. Sutton, R.W. Balluffi, Interfaces in crystalline materials. http://catalog.hathitrust.org/api/volumes/oclc/31166519.html, 1995).
[11] T. Frolov, D.L. Olmsted, M. Asta, Y. Mishin, Structural phase transformations in metallic grain boundaries, Nat Commun 4 (2013) 1899.
[12] Q. Zhu, A. Samanta, B. Li, R.E. Rudd, T. Frolov, Predicting phase behavior of grain boundaries with evolutionary search and machine learning, Nat Commun 9 (1) (2018) 467.
[13] A. Kashinath, A. Misra, M.J. Demkowicz, Stable Storage of Helium in Nanoscale Platelets at Semicoherent Interfaces, Phys. Rev. Lett. 110 (8) (2013) 086101.
[14] A. Vattré, T. Jourdan, H. Ding, M.C. Marinica, M.J. Demkowicz, Non-random walk diffusion enhances the sink strength of semicoherent interfaces, Nat Commun 7 (2016) 10424.
[15] J. Han, V. Vitek, D.J. Srolovitz, Grain-boundary metastability and its statistical properties, Acta Mater 104 (2016) 259–273.
[16] G.H. Balbus, M.P. Echlin, C.M. Grigorian, T.J. Rupert, T.M. Pollock, D.S. Gianola, Femtosecond laser rejuvenation of nanocrystalline metals, Acta Mater 156 (2018) 183–195.
[17] Y. Mishin, M.J. Mehl, D.A. Papaconstantopoulos, A.F. Voter, J.D. Kress, Structural stability and lattice defects in copper: ab initio, tight-binding, and embedded-atom calculations, Phys. Rev. B 63 (22) (2001) 224106.
[18] M.A. Tschopp, S.P. Coleman, D.L. McDowell, Symmetric and asymmetric tilt grain boundary structure and energy in Cu and Al (and transferability to other fcc metals), Integrating Materials and Manufacturing Innovation 4 (1) (2015) 11.
[19] E. Cances, F. Legoll, M.C. Marinica, K. Minoukadeh, F. Willaime, Some improvements of the activation-relaxation technique method for finding transition pathways on potential energy surfaces, Journal of Chemical Physics 130 (11) (2009) 114711.
[20] H. Zhang, D.J. Srolovitz, Simulation and analysis of the migration mechanism of Σ5 tilt grain boundaries in an fcc metal, Acta Mater 54 (3) (2006) 623–633.
[21] L. Zhong, J. Wang, H. Sheng, Z. Zhang, S.X. Mao, Formation of monatomic metallic glasses through ultrafast liquid quenching, Nature 512 (7513) (2014) 177–180.
[22] P.G. Debenedetti, F.H. Stillinger, Supercooled liquids and the glass transition, Nature 410 (6825) (2001) 259–267.
[23] S. Sastry, P.G. Debenedetti, F.H. Stillinger, Signatures of distinct dynamical regimes in the energy landscape of a glass-forming liquid, Nature 393 (6685) (1998) 554–557.
[24] F.H. Stillinger, A Topographic View of Supercooled Liquids and Glass Formation, Science 267 (5206) (1995) 1935–1939.
[25] Y.Q. Cheng, E. Ma, Atomic-level structure and structure–property relationship in metallic glasses, Prog Mater Sci 56 (4) (2011) 379–473.
[26] D.J. Wales, A Microscopic Basis for the Global Appearance of Energy Landscapes, Science 293 (5537) (2001) 2067–2070.

[27] D.J. Wales, Decoding the energy landscape: extracting structure, dynamics and thermodynamics, Philosophical Transactions of the Royal Society A: mathematical, Physical and Engineering Sciences 370 (1969) (2012) 2877–2899.
[28] Y. Fan, B. Yildiz, S. Yip, Analogy between glass rheology and crystal plasticity: yielding at high strain rate, Soft Matter 9 (40) (2013) 9511–9514.
[29] C. Liu, X. Yan, P. Sharma, Y. Fan, Unraveling the non-monotonic ageing of metallic glasses in the metastability-temperature space, Computational Materials Science 172 (2020) 109347.
[30] Y. Fan, T. Iwashita, T. Egami, Energy landscape-driven non-equilibrium evolution of inherent structure in disordered material, Nat Commun 8 (2017) 15417.
[31] A.C. Lund, C.A. Schuh, Strength asymmetry in nanocrystalline metals under multiaxial loading, Acta Mater 53 (11) (2005) 3193–3205.
[32] A. Khalajhedayati, T.J. Rupert, Emergence of localized plasticity and failure through shear banding during microcompression of a nanocrystalline alloy, Acta Mater 65 (2014) 326–337.
[33] H. Van Swygenhoven, M. Spaczer, A. Caro, D. Farkas, Competing plastic deformation mechanisms in nanophase metals, Physical Review B 60 (1) (1999) 22–25.
[34] H. Zhang, D.J. Srolovitz, J.F. Douglas, J.A. Warren, Grain boundaries exhibit the dynamics of glass-forming liquids, Proceedings of the National Academy of Sciences 106 (19) (2009) 7735–7740.
[35] T.A. Sharp, S.L. Thomas, E.D. Cubuk, S.S. Schoenholz, D.J. Srolovitz, A.J. Liu, Machine learning determination of atomic dynamics at grain boundaries, Proceedings of the National Academy of Sciences 115 (43) (2018) 10943.
[36] K.C. Alexander, C.A. Schuh, Exploring grain boundary energy landscapes with the activation-relaxation technique, Scr Mater 68 (12) (2013) 937–940.
[37] D. Rodney, C. Schuh, Distribution of Thermally Activated Plastic Events in a Flowing Glass, Phys. Rev. Lett. 102 (23) (2009) 235503.
[38] H. Kallel, N. Mousseau, F. Schiettekatte, Evolution of the Potential-Energy Surface of Amorphous Silicon, Phys. Rev. Lett. 105 (4) (2010) 045503.
[39] C. Liu, P. Guan, Y. Fan, Correlating defects density in metallic glasses with the distribution of inherent structures in potential energy landscape, Acta Mater 161 (2018) 295–301.
[40] B. Schönfelder, D. Wolf, S.R. Phillpot, M. Furtkamp, Molecular-Dynamics Method for the Simulation of Grain-Boundary Migration, Interface Science 5 (4) (1997) 245–262.
[41] M.R. Sørensen, Y. Mishin, A.F. Voter, Diffusion mechanisms in Cu grain boundaries, Physical Review B 62 (6) (2000) 3658–3673.
[42] N.Q. Vo, J. Schäfer, R.S. Averback, K. Albe, Y. Ashkenazy, P. Bellon, Reaching theoretical strengths in nanocrystalline Cu by grain boundary doping, Scr Mater 65 (8) (2011) 660–663.
[43] L. Zhang, C. Lu, Y. Shibuta, Shear response of grain boundaries with metastable structures by molecular dynamics simulations, Modelling and Simulation in Materials Science and Engineering 26 (3) (2018) 035008.
[44] C. Wu, M.S. Christensen, J.-M. Savolainen, P. Balling, L.V. Zhigilei, Generation of subsurface voids and a nanocrystalline surface layer in femtosecond laser irradiation of a single-crystal Ag target, Physical Review B 91 (3) (2015) 035413.
[45] C. Wu, L.V. Zhigilei, Nanocrystalline and Polyicosahedral Structure of a Nanospike Generated on Metal Surface Irradiated by a Single Femtosecond Laser Pulse, The Journal of Physical Chemistry C 120 (8) (2016) 4438–4447.
[46] M. Gill-Comeau, L.J. Lewis, Ultrashort-pulse laser ablation of nanocrystalline aluminum, Physical Review B 84 (22) (2011) 224110.
[47] O. Renk, A. Hohenwarter, K. Eder, K.S. Kormout, J.M. Cairney, R. Pippan, Increasing the strength of nanocrystalline steels by annealing: is segregation necessary? Scr Mater 95 (2015) 27–30.
[48] X. Huang, N. Hansen, N. Tsuji, Hardening by Annealing and Softening by Deformation in Nanostructured Metals, Science 312 (5771) (2006) 249–251.
[49] L. Chang, P.W. Kao, C.H. Chen, Strengthening mechanisms in electrodeposited Ni–P alloys with nanocrystalline grains, Scr Mater 56 (8) (2007) 713–716.
[50] X. Zhou, X.Y. Li, K. Lu, Enhanced thermal stability of nanograined metals below a critical grain size, Science 360 (6388) (2018) 526–530.
[51] H.A. Khater, A. Serra, R.C. Pond, J.P. Hirth, The disconnection mechanism of coupled migration and shear at grain boundaries, Acta Mater 60 (5) (2012) 2007–2020.
[52] G.J. Tucker, M.A. Tschopp, D.L. McDowell, Evolution of structure and free volume in symmetric tilt grain boundaries during dislocation nucleation, Acta Mater 58 (19) (2010) 6464–6473.
[53] S.L. Thomas, K. Chen, J. Han, P.K. Purohit, D.J Srolovitz, Reconciling grain growth and shear-coupled grain boundary migration, Nat Commun 8 (1) (2017) 1764.
[54] D.L. Olmsted, D. Buta, A. Adland, S.M. Foiles, M. Asta, A. Karma, Dislocation–Pairing Transitions in Hot Grain Boundaries, Phys. Rev. Lett. 106 (4) (2011) 046101.
[55] J.-P. Du, Y.-J. Wang, Y.-C. Lo, L. Wan, S. Ogata, Mechanism transition and strong temperature dependence of dislocation nucleation from grain boundaries: an accelerated molecular dynamics study, Physical Review B 94 (10) (2016) 104110.
[56] T.J. Rupert, C.A. Schuh, Mechanically driven grain boundary relaxation: a mechanism for cyclic hardening in nanocrystalline Ni, Philos Mag Lett 92 (1) (2012) 20–28.
[57] N.Q. Vo, R.S. Averback, P. Bellon, A. Caro, Yield strength in nanocrystalline Cu during high strain rate deformation, Scr Mater 61 (1) (2009) 76–79.
[58] D. Utt, A. Stukowski, K. Albe, Grain boundary structure and mobility in high--entropy alloys: a comparative molecular dynamics study on a Σ11 symmetrical tilt grain boundary in face-centered cubic CuNiCoFe, Acta Mater 186 (2020) 11–19.
[59] J. Schiøtz, T. Vegge, F.D. Di Tolla, K.W. Jacobsen, Atomic-scale simulations of the mechanical deformation of nanocrystalline metals, Physical Review B 60 (17) (1999) 11971–11983.
[60] W.C. Oliver, G.M. Pharr, An improved technique for determining hardness and elastic modulus using load and displacement sensing indentation experiments, J Mater Res 7 (6) (1992) 1564–1583.